



Article

# Facile Synthesis of MnO<sub>2</sub> Nanoflowers/N-Doped Reduced Graphene Oxide Composite and Its Application for Simultaneous Determination of Dopamine and Uric Acid

Xuan Wan <sup>1,†</sup>, Shihui Yang <sup>1,†</sup>, Zhaotian Cai <sup>1</sup>, Quanguo He <sup>1</sup>, Yabing Ye <sup>1</sup>, Yonghui Xia <sup>2</sup>, Guangli Li <sup>1,\*</sup> and Jun Liu <sup>1,\*</sup>

<sup>1</sup> College of Life Sciences and Chemistry, Hunan University of Technology, Zhuzhou 412007, China; wanxuan1111@163.com (X.W.); yangshihui0522@163.com (S.Y.); caizhaotian1998@163.com (Z.C.); hequanguo@126.com (Q.H.); yyb980501@163.com (Y.Y.)

<sup>2</sup> Zhuzhou Institute for Food and Drug Control, Zhuzhou 412000, China; Sunnyxia0710@163.com

\* Correspondence: guangli010@hut.edu.cn (G.L.); junliu@hut.edu.cn (J.L.);  
Tel.: +86-0731-2218-3382 (G.L. & J.L.)

† These authors contributed equally to this work.

Received: 13 May 2019; Accepted: 28 May 2019; Published: 2 June 2019



**Abstract:** This study reports facile synthesis of MnO<sub>2</sub> nanoflowers/N-doped reduced graphene oxide (MnO<sub>2</sub>NFs/NrGO) composite and its application on the simultaneous determination of dopamine (DA) and uric acid (UA). The microstructures, morphologies, and electrochemical performances of MnO<sub>2</sub>NFs/NrGO were studied using X-ray diffraction (XRD), scanning electron microscopy (SEM), cyclic voltammetry (CV), and electrochemical impedance spectroscopy (EIS), respectively. The electrochemical experiments showed that the MnO<sub>2</sub>NFs/NrGO composites have the largest effective electroactive area and lowest charge transfer resistance. MnO<sub>2</sub>NFs/NrGO nanocomposites displayed superior catalytic capacity toward the electro-oxidation of DA and UA due to the synergistic effect from MnO<sub>2</sub>NFs and NrGO. The anodic peak currents of DA and UA increase linearly with their concentrations varying from 0.2 μM to 6.0 μM. However, the anodic peak currents of DA and UA are highly correlated to the Napierian logarithm of their concentrations ranging from 6.0 μM to 100 μM. The detection limits are 0.036 μM and 0.029 μM for DA and UA, respectively. Furthermore, the DA and UA levels of human serum samples were accurately detected by the proposed sensor. Combining with prominent advantages such as facile preparation, good sensitivity, and high selectivity, the proposed MnO<sub>2</sub>NFs/NrGO nanocomposites have become the most promising candidates for the simultaneous determination of DA and UA from various actual samples.

**Keywords:** dopamine; uric acid; MnO<sub>2</sub> nanoflowers; N-doped reduced graphene oxide; voltammetric sensor

## 1. Introduction

Dopamine (DA) and uric acid (UA) often coexist in the biological fluids, such as blood serum, urine, and extracellular fluids, which play a vitally significant role on the regulation of human physiological functions and metabolic activities [1]. As an essential catecholamine neurotransmitter, DA plays a pivotal role in regulating the functions of cardiovascular and central nervous systems, adjusting emotions, and maintaining hormonal balances [2]. The dysfunction of DA possibly causes many neurological disorders like Parkinson's syndrome, Alzheimer's diseases, and schizophrenia [3–5]. For a healthy individual, the DA levels in biological matrixes generally vary from 0.01 μM to 1 μM. The response signals of DA are often susceptible to interferences from endogenous biomolecules i.e.,

ascorbic acid (AA) and UA. Therefore, it remains a great challenge for the fast and precise detection of DA. As another critical biomolecule in human body, UA is commonly regarded as the metabolic product of purine [6]. Generally, the UA level is  $4.1 \pm 8.8$  mg/100 mL for a healthy individual [7]. The abnormal concentration of UA in physiological fluids likely leads to several disorders including pneumonia, hyperuricemia, and gout [8]. Thus, the levels of DA and UA in physiological fluids have become important indicators or biomarkers for healthcare and clinical diagnosis. Therefore, it is extremely necessary to propose some efficient and reliable approaches toward the simultaneous determination of DA and UA.

Up until now, various detection approaches have been reported for detecting DA and UA, such as chemiluminescent [9], HPLC [10,11], fluorometry [12], spectrophotometry [13], and surface plasmon resonance [14]. These techniques are very reliable, but they often involve cumbersome and time-consuming procedures that require large instruments, experienced technicians, and even a large amount of poisonous solvents [15]. Recently, electrochemical approaches have drawn growing attention for the determination of bioactive compounds, food dyes, and pollutants, owing to their considerable advantages such as being inexpensive, facial operation, high efficiency, good selectivity, and sensitivity [16–20]. In addition, DA and UA are highly electroactive biomolecules, which are more suitable for electrochemical detection. However, bare electrodes often suffer from electrode fouling and cross-interference issues, which result in poor sensitivity and reproducibility [7,21]. To address the issues, various nanomaterials were developed to construct electrochemical sensors.

As a versatile transition metal oxide,  $\text{MnO}_2$  has been intensively utilized in energy storage, catalysis, and sensors because of its peculiar properties including low-cost, more abundance, high-catalytic activity, and environmental friendliness. Until now, a variety of nanostructured  $\text{MnO}_2$  such as nanowires [16,22], nanorods [17,23,24], nanotubes [25,26], microspheres [27,28], and nanoflowers [29,30] have been prepared, characterized, and even used in electrochemical determination. Among these morphologies,  $\text{MnO}_2$  nanoflowers ( $\text{MnO}_2\text{NFs}$ ) have drawn considerable attention, attributing to their pore structure and large specific surface area. As sensing materials,  $\text{MnO}_2$  nanoflowers have been used for the detection of lead ion [29], ractopamine [30], salbutamol [30], guaiacol [31], vanillin [31], hydrogen peroxide [32], and DA [33]. These studies demonstrate that  $\text{MnO}_2$  nanoflowers improve the electrochemical performances significantly. But their poor dispersibility and electrical conductivity have impeded widespread applications in electrochemical sensors.

To resolve this problem, an effective strategy is to composite nanostructured  $\text{MnO}_2$  with graphene materials, which not only effectively improve the dispersibility, but also endow a synergistic effect towards sensing target analytes. However, the electrical conductivity of graphene cannot be fully controlled due to the lack of bandgap [34]. In this regard, many approaches have been proposed to modify the electron transfer and surface chemical properties, among which the doping of nitrogen into graphene has displayed enormous potential for widespread applications [35]. Compared to pristine graphene, N-doped reduced graphene oxide (NrGO) possesses a more biocompatible C-N microenvironment, a much larger functional surface area, a better electrical conductivity, a higher ratio of surface-active groups to volume, and enhanced electrocatalytic effects [35,36]. Therefore, NrGO has been widely used to construct a variety of electrochemical sensors. For example, Yang and coworkers [37] reported a facile one-step hydrothermal preparation of  $\text{Fe}_2\text{O}_3/\text{NrGO}$  nanohybrids toward DA detection.  $\text{Fe}_2\text{O}_3/\text{NrGO}$  showed superior electrocatalytic activity toward DA oxidation, with a broad detection range (0.5  $\mu\text{M}$ –0.34 mM), a low limit of detection (LOD, 0.49  $\mu\text{M}$ ), and good sensitivity (418.6  $\mu\text{A mM}^{-1} \text{cm}^{-2}$ ). Chen et al. [38] prepared NrGO/MnO nanocomposite via the freeze-drying technique to construct a selective electrochemical sensor for the detection of DA in the coexistence of UA and AA. Although NrGO has been intensively utilized in electrochemical sensing, as far as we know there is no report available for the use of  $\text{MnO}_2/\text{N}$ -doped graphene composite for the simultaneous detection of DA and UA.

Herein, MnO<sub>2</sub>NFs/NrGO nanocomposites were prepared by a facile, cost-effective and highly efficient route rather than the conventional hydrothermal method. Specifically, MnO<sub>2</sub>NFs were prepared by a slow addition of MnSO<sub>4</sub> into KMnO<sub>4</sub> solution followed by a simple stirring procedure, then composited with NrGO nanosheets with an ultrasonication assistant. The combined virtues of MnO<sub>2</sub>NFs and NrGO nanosheets are expected to enhance electrochemical sensing properties, which has been proven by using the MnO<sub>2</sub>NFs/NrGO as an efficient electrocatalyst for the simultaneous determination of DA and UA in serum samples. The proposed sensor showed remarkable catalytic capacity toward the oxidation of DA and UA, with two detection ranges (0.2–6.00 μM and 6–100 μM), low LOD (36 and 29 nM for DA and UA respectively), and good selectivity as well as reproducibility.

## 2. Materials and Methods

### 2.1. Reagents

UA, DA, NaH<sub>2</sub>PO<sub>4</sub>, and Na<sub>2</sub>HPO<sub>4</sub> were purchased from Aladdin Reagents Co., Ltd. (Shanghai, China). K<sub>4</sub>[Fe(CN)<sub>6</sub>], K<sub>3</sub>[Fe(CN)<sub>6</sub>], MnSO<sub>4</sub>, KMnO<sub>4</sub>, NaOH, H<sub>3</sub>PO<sub>4</sub>, and absolute ethanol were supplied by Sinopharm Chemical Reagent Co. Ltd. (Shanghai, China). All of the chemicals were analytically pure and used as received. NrGO was supplied by Nanjing Xianfeng NANO Material Tech Co. Ltd. (Nanjing, China). Human serum samples were provided by Zhuzhou People's Hospital (Zhuzhou, China). The human samples are a mixture of residual serum from various individuals after clinical examination. Deionized water with the resistivity of 18.2 MΩ was used in all of the experiments.

### 2.2. Materials Characterization

Crystalline structures and surface morphologies of MnO<sub>2</sub>NFs and MnO<sub>2</sub>NFs/NrGO were investigated by powder X-ray diffractometry (XRD) and scanning electron microscopy (SEM), respectively. SEM images were taken from a cold field-emission SEM (Hitachi S-4800, Tokyo, Japan). The XRD patterns of MnO<sub>2</sub>NFs were collected using a powder XRD system (PANalytical, Almelo, The Netherlands) with monochromatized Cu Kα radiation (λ = 0.1542 nm), which was operated at 40 kV and 40 mA.

### 2.3. Synthesis of MnO<sub>2</sub>NFs/NNrGO Composites

The MnO<sub>2</sub>NFs was prepared by a slow addition of MnSO<sub>4</sub> into KMnO<sub>4</sub> solution followed by a simple stirring procedure. Typically, 1 mmol of KMnO<sub>4</sub> and 1.5 mmol of MnSO<sub>4</sub> were adequately dissolved into 20 mL deionized water, separately. Then, the MnSO<sub>4</sub> solution was added dropwise into KMnO<sub>4</sub> solution at a rate of 1 mL min<sup>-1</sup>, and agitated continuously at room temperature for 2 h. The resultant product was collected by centrifugation at 12,000 rpm, followed by cleaning alternately with absolute alcohol and deionized water three times, and dried at 60 °C in a vacuum oven overnight. Obviously, this route is time-saving and more convenient when compared with the conventional hydrothermal method.

MnO<sub>2</sub>NFs/NrGO composites were prepared as follows. Firstly, 10 mg MnO<sub>2</sub>NFs were uniformly dispersed in 10 mL deionized water under an ultrasonication bath for 0.5 h. Then 0.2 g NrGO nanosheets were added into the above MnO<sub>2</sub>NFs dispersion (1 mg mL<sup>-1</sup>) and dispersed under ultrasonication for 1 h. The MnO<sub>2</sub>NFs/NrGO were stored at 4 °C in a refrigerator when not used. To ensure good reproducibility, the MnO<sub>2</sub>NFs/NrGO were subjected to ultrasonication for 0.5 h before each modification.

### 2.4. Fabrication of MnO<sub>2</sub>NFs/NrGO Modified Electrodes

The bare glassy carbon electrodes (GCEs) were carefully polished using 0.3 μm and 0.05 μm alumina slurry, then alternately washed by anhydrous alcohol and deionized water several times, and allowed to dry under an infrared lamp. The MnO<sub>2</sub>NFs/NrGO-modified GCE (MnO<sub>2</sub>NFs/NrGO/GCE) was prepared via a simple drop-casting approach. Specifically, 5 μL MnO<sub>2</sub>NFs/NrGO dispersion was

carefully dropped and casted on the GCE surface with a micropipette, then dried with an infrared lamp to form a sensing film. For comparison, MnO<sub>2</sub>NFs and NrGO-modified GCEs (MnO<sub>2</sub>NFs/GCE, NrGO/GCE) were also prepared via similar procedures.

### 2.5. Procedures for Electrochemical Measurements

For all the electrochemical tests, a typical three-electrode assemble was immersed into a 10 mL electrochemical cell, in which a bare or modified GCE was worked as the working electrode. Saturated calomel electrode (SCE) and platinum wire were used as a reference electrode and auxiliary electrode, respectively. To evaluate the electrochemical performance of various modified electrodes, cyclic voltammetry (CV) and electrochemical impedance spectroscopy (EIS) was measured in the 0.1 M phosphate buffered solution (PBS, pH 7.0), using 0.5 mM [Fe(CN)<sub>6</sub>]<sup>3-/4-</sup> as redox probe couples. EIS plots for different electrodes were recorded at open circuit potential using 5 mV (rms) AC sinusoid signal at a frequency range from 100,000 Hz to 0.1 Hz. The voltammetric responses of 10 μM DA and UA at different electrodes were tested by CV. After a suitable accumulation, linear scanning voltammetry (LSV) was performed for the determination of DA and UA. The potentials were scanned from 0 V to 0.8 V at 100 mVs<sup>-1</sup> for both CV and LSV.

## 3. Results and Discussion

### 3.1. Physical Characterization

The crystalline structure of MnO<sub>2</sub> nanoflowers was characterized by XRD. As presented in Figure 1, sharp diffraction peaks were observed at 2θ of 12.94°, 18.34°, 28.78°, 37.66°, 42.14°, 49.90°, 56.44°, 60.26°, 69.74°, 71.34°, and 73.72°, which can be well-indexed into (110), (200), (310), (211), (301), (411), (600), (521), (541), (222), and (730) facets, respectively. It is in good agreement with XRD standard card JSPDF 44-0141 [16,17], suggesting tetragonal crystalline of α-MnO<sub>2</sub> were successfully synthesized. Moreover, no visible peak relating to impurities appears, indicating high-purity of α-MnO<sub>2</sub>. SEM images of MnO<sub>2</sub>NFs are shown in Figure 2A, B. Obviously, flower-like nanostructures composed of interconnected nanoflakes suggests MnO<sub>2</sub> nanoflowers were successfully synthesized. The porous microstructures indicate that MnO<sub>2</sub> nanoflowers have a large specific surface area, which is favorable for electrochemical sensing. As shown in Figure 2C,D, the NrGO nanosheets were warped on the surface of MnO<sub>2</sub>NFs, suggesting MnO<sub>2</sub>NFs/NrGO nanocomposites were successfully prepared.

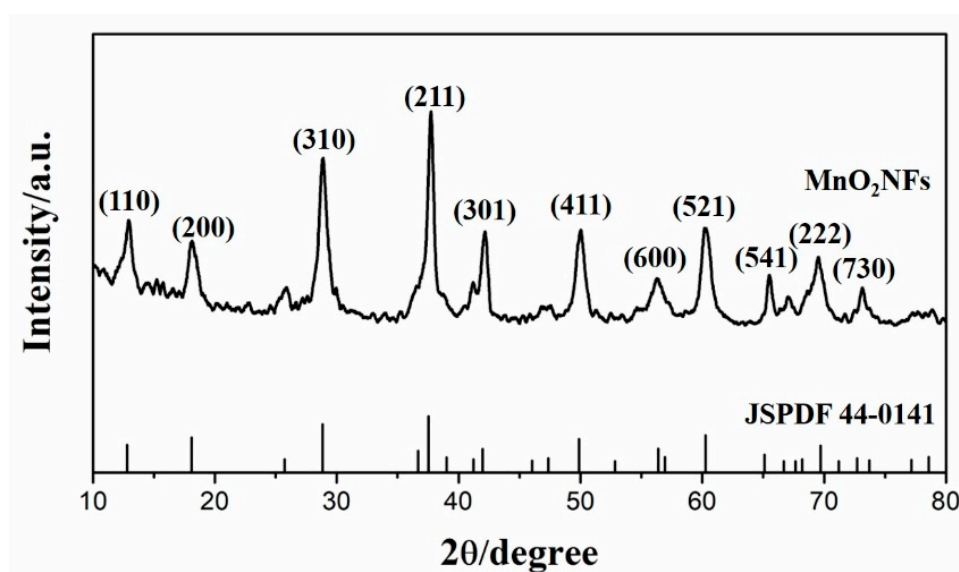
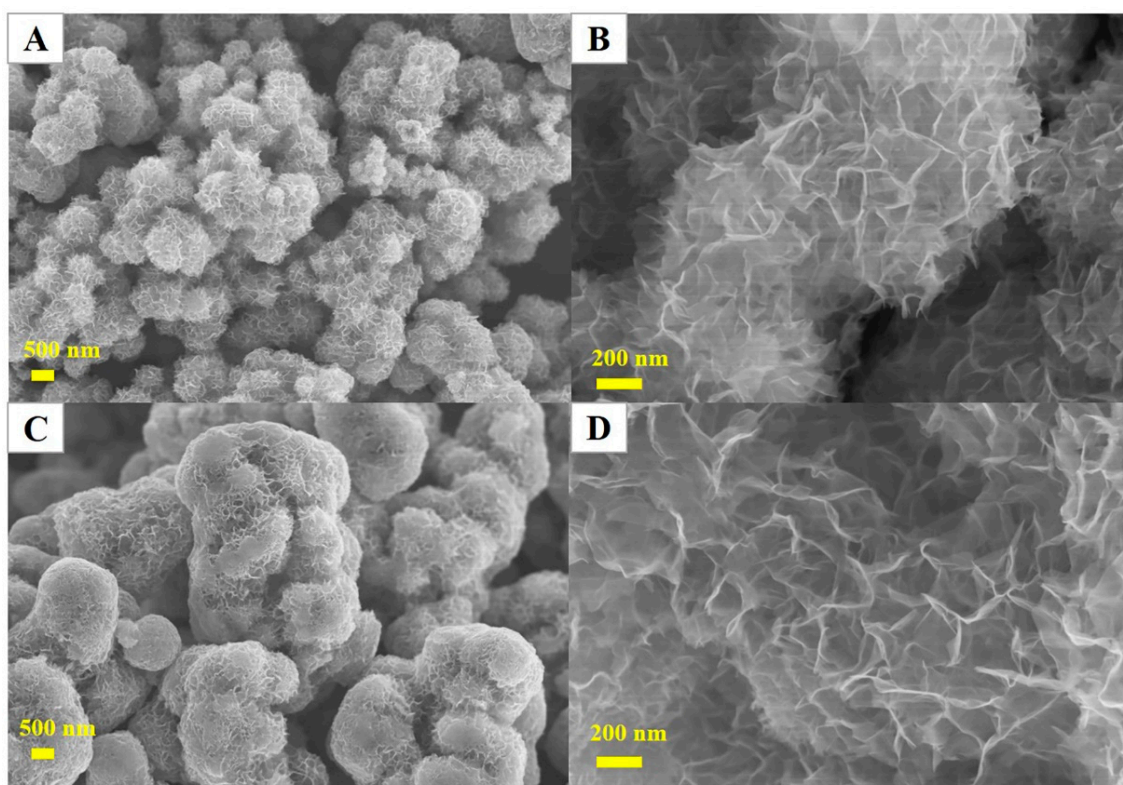


Figure 1. X-ray diffraction (XRD) patterns of MnO<sub>2</sub> nanoflowers and standard card JSPDF 44-0141.



**Figure 2.** Scanning electron microscopy (SEM) images of MnO<sub>2</sub>NFs (A,B) and MnO<sub>2</sub>NFs/NrGO nanocomposites (C,D) at different magnifications.

### 3.2. Evaluation of Electrochemical Performances

In order to assess the electrochemical performances, CVs for various modified electrodes were measured in a mixture solution of 0.5 mM [Fe(CN)<sub>6</sub>]<sup>3-/4-</sup> and 0.1 M KCl (Figure 3A). A pair of quasi-reversible redox peaks occurred on all of the electrodes with  $i_{pa}/i_{pc} \approx 1.0$ . At bare GCE, a pair of weak redox appeared with the anodic and cathodic peak current of 12.23 and 9.02  $\mu\text{A}$ , respectively. After the modification of GCE by MnO<sub>2</sub>NFs or NrGO, the redox peak currents increased by 2-fold approximately. As expected, a well-defined and sharp redox peak was observed at the MnO<sub>2</sub>NFs/NrGO/GCE, with the highest anodic and cathodic peak currents ( $i_{pa} = 92.41 \mu\text{A}$ ,  $i_{pc} = 87.89 \mu\text{A}$ ). It indicates that MnO<sub>2</sub>NFs/NrGO significantly improved electrochemical performances. It is well-known that the effective electroactive area is a critical factor that directly influences the electrochemical sensing performances. The effective electroactive areas of different electrodes were also calculated, using the *Randles–Sevcik* equation as follows [16,17,20]:

$$i_{pc} = (2.69 \times 10^5) n^{3/2} D^{1/2} v^{1/2} AC \quad (1)$$

where  $i_{pc}$  represents the cathodic peak current (A),  $n$  represents the electron transfer number,  $D$  represents the diffusion coefficient of K<sub>3</sub>[Fe(CN)<sub>6</sub>] ( $7.6 \times 10^{-6} \text{ cm}^2 \text{ s}^{-1}$  [39]),  $v$  denotes the scanning rate ( $\text{V s}^{-1}$ ),  $A$  denotes the effective electroactive area ( $\text{cm}^2$ ), and  $C$  denotes the K<sub>3</sub>[Fe(CN)<sub>6</sub>] concentration ( $\text{mol cm}^{-3}$ ). The effective electroactive areas were estimated to be 0.0770, 0.3183, 0.3958, and 0.7496  $\text{cm}^2$  for the bare GCE, MnO<sub>2</sub>NFs/GCE, NrGO/GCE, and MnO<sub>2</sub>NFs/NrGO/GCE, respectively. The effective electroactive area of MnO<sub>2</sub>NFs/NrGO/GCE is about 9-fold higher than that of the bare GCE approximately. The results suggest that the MnO<sub>2</sub>NFs/NrGO nanocomposites significantly enlarged the effective electroactive surface area, which promoted the accumulation of target analysts and thus increased the response electrochemical signals.

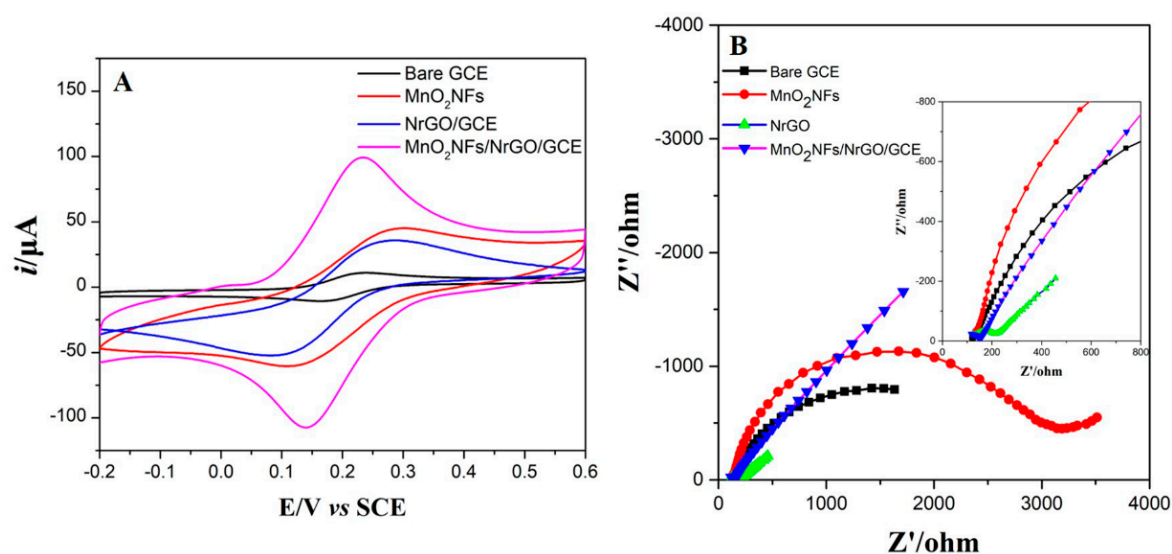


**Figure 3.** Cyclic voltammetry (CVs) (A) and Nyquist plots (B) for various electrodes in 0.5 mM  $[\text{Fe}(\text{CN})_6]^{3-/4-}$  containing 0.1 M KCl solution. The inset in Figure 3B represents the magnification of Nyquist at a higher frequency.

EIS has intensively been used to investigate interfacial properties of various electrochemical sensors [16,17,40–42]. Nyquist plots for various electrodes are plotted in Figure 3B. Obviously, Nyquist plots comprise of the semicircular at higher frequencies relating to the electron transfer-limited process, and linear portions at lower frequencies corresponding to the diffusion-controlled process. The semicircular diameter represents the charge transfer resistance ( $R_{ct}$ ). The  $R_{ct}$  values for the bare GCE,  $\text{MnO}_2/\text{NFs}/\text{GCE}$ ,  $\text{NrGO}/\text{GCE}$ , and  $\text{MnO}_2/\text{NFs}/\text{NrGO}/\text{GCE}$  are 1950, 2551, 72.47, and 25.28 ohm, respectively. After modification with  $\text{MnO}_2/\text{NFs}$ , the  $R_{ct}$  value increased by 601 ohm because of the poor electro-conductivity of  $\text{MnO}_2$ . When GCE was modified with NrGO, the  $R_{ct}$  significantly decreased to 74.25 ohm, which can attribute to the good electro-conductivity and high-specific surface area of NrGO [35,36]. As expected, the lowest  $R_{ct}$  value was obtained at  $\text{MnO}_2/\text{NFs}/\text{NrGO}/\text{GCE}$ , probably due to the existence of abundant electrocatalytic active sites that can greatly accelerate the redox reaction of  $[\text{Fe}(\text{CN})_6]^{3-/4-}$ . The results demonstrate that the  $\text{MnO}_2/\text{NFs}/\text{NrGO}$  can effectively decrease the  $R_{ct}$ .

### 3.3. Voltammetric Responses of DA and UA at Various Electrodes

CV responses of 10  $\mu\text{M}$  DA and UA (1:1) were measured at different electrodes in 0.1 M PBS (pH 3.93) (Figure 4). When the potentials were scanned from 0 to 0.8 V, two anodic peaks were observed at all electrodes, which are closely related to the oxidation of DA and UA. However, only one peak belonging to the reduction of DA occurred at reverse scanning. These phenomena indicate that the electrooxidation of UA is totally irreversible. On the bare GCE, two very weak anodic peaks appeared ( $i_{pa}(\text{DA}) = 1.126 \mu\text{A}$ ,  $i_{pa}(\text{UA}) = 0.385 \mu\text{A}$ ), demonstrating sluggish kinetics for the electrooxidation of DA and UA. After modification of the GCE by  $\text{MnO}_2/\text{NFs}$ , the  $i_{pa}(\text{DA})$  increased a little ( $i_{pa}(\text{DA}) = 3.766 \mu\text{A}$ ) while the  $i_{pa}(\text{UA})$  was enhanced significantly ( $i_{pa}(\text{UA}) = 12.73 \mu\text{A}$ ), showing  $\text{MnO}_2/\text{NFs}$  have good electrocatalytic toward the oxidation of UA because of the presence of  $\text{Mn}^{4+}/\text{Mn}^{3+}$  as an electron mediator. Moreover, the high-specific surface area also contributed to the obvious enhancement on the  $i_{pa}(\text{UA})$ . When GCE was modified with NrGO, the  $i_{pa}(\text{DA})$  and  $i_{pa}(\text{UA})$  increased to 7.029  $\mu\text{A}$  and 16.43  $\mu\text{A}$  respectively, suggesting superb electrocatalytic activity toward the oxidation of DA and UA. The superb electrocatalytic activity of NrGO can explain the following facts. Nitrogen atoms

in NrGO sheets may interact with target biomolecules via hydrogen bond, which can activate the amine and hydroxy groups and expedite the charge transfer process. Meanwhile, the  $\pi$ - $\pi$  interactions between NrGO and target biomolecules can also facilitate the charge transfer process [43]. Two sharp anodic peaks occurred at MnO<sub>2</sub>NFs/NrGO/GCE, and the anodic peak currents enhanced remarkably ( $i_{pa}(DA) = 14.8 \mu A$ ,  $i_{pa}(UA) = 36.3 \mu A$ ). The synergistic effect between MnO<sub>2</sub>NFs and NrGO sheets was mainly responsible for the enhanced response peak currents. Specially, MnO<sub>2</sub>NFs had higher catalytic activity toward the oxidation of DA and UA when the electrical conductivity was improved by coupling with NrGO sheets. Meanwhile, the hydrogen bond and  $\pi$ - $\pi$  interactions between NrGO sheets and target biomolecules can also facilitate the charge transfer process. It is worth noting the biggest peak potential separation (about 150 mV) at MnO<sub>2</sub>NFs/NrGO/GCE, rendering this composite more selective for the simultaneous detection of UA and DA. Besides, the largest background current was also obtained at the MnO<sub>2</sub>NFs/NrGO nanocomposites, due to the high-specific capacitance of the MnO<sub>2</sub>NFs/NrGO nanocomposites [44].

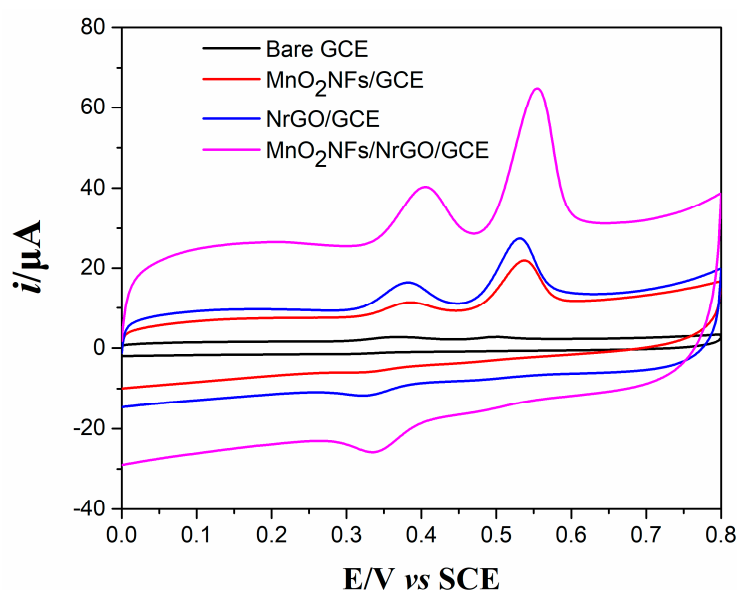


**Figure 4.** CVs of 10  $\mu M$  Dopamine (DA) and uric acid (UA) mixture solution (1:1) on different electrodes.

### 3.4. Optimization of Voltammetrical Parameters

#### 3.4.1. Effect of pH

As known to all, the voltammetric responses of DA and UA highly depend on the solution pH. Therefore, it's worthwhile to optimize pH. The dependences of pH on the anodic peak currents of DA and UA are shown in Figure 5A. In the pH range of 2.58 to 3.93, the  $i_{pa}(DA)$  gradually increased with the increase of pH, then decreased slowly as the pH rose to 7.01, and suddenly decreased when the pH exceeded 7.01. Obviously, the maximal  $i_{pa}(DA)$  was achieved at pH 3.93. As for UA, the  $i_{pa}(UA)$  show a downward trend, with pH varying from 2.58 to 8.52. To ensure the highest possible anodic peak current for DA and UA, pH 3.93 was selected for the following experiments. Moreover, the anodic peak potentials of DA and UA linearly decreased as pH was rising (Figure 5B). The linear relationships of  $E_{pa}$  versus pH can be expressed as  $E_{pa}(DA) = -0.0685 \text{ pH} + 0.839$  ( $R^2 = 0.974$ ) and  $E_{pa}(UA) = -0.0639 \text{ pH} + 0.679$  ( $R^2 = 0.976$ ), respectively. Their slopes (68.5 pH/mV and 63.9 pH/mV) are close to 59 mV/pH, demonstrating the equal numbers of electron ( $e^-$ ) and protons ( $H^+$ ) involved

in their electrooxidation processes [16]. As reported, the oxidation of DA and UA are two electron transfer processes [45]. Hence, the electrooxidation of DA and UA involves two electrons ( $2e^-$ ) and two protons ( $2H^+$ ). The electrochemical oxidation process of DA and UA at the  $MnO_2NFs/NrGO/GCE$  are illustrated in Scheme 1.

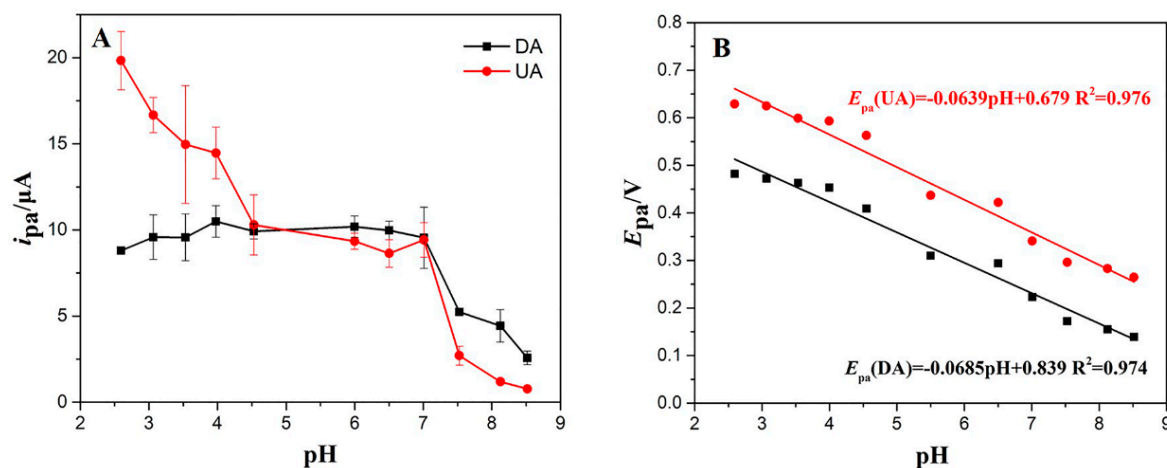
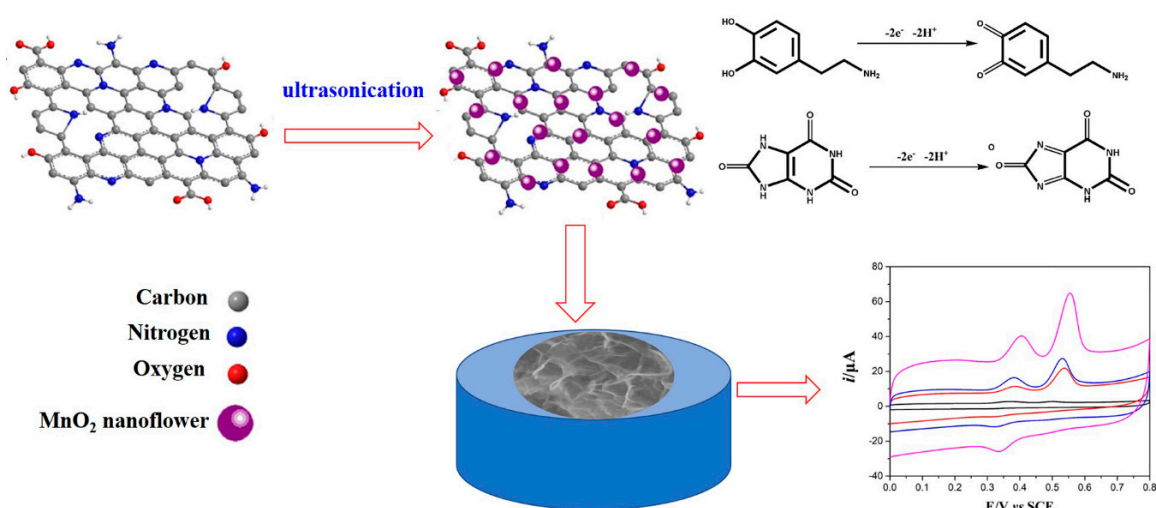


**Figure 5.** (A) Dependence of pH on the anodic peak currents of DA and UA. (B) Linear plots of anodic peak potentials of DA and UA against pH ( $n = 3$ ).



**Scheme 1.** Scheme diagram of the electrochemical oxidation of DA and UA at the  $MnO_2NFs/NrGO/GCE$ .

### 3.4.2. Effect of Scanning Rate

In order to give a deep insight into the oxidation of DA and UA, CVs of 10  $\mu M$  DA and UA were performed at various scanning rates (Figure 6A). As the scanning rates increased, their anodic peaks shifted positively while the cathodic peaks shifted in the reverse direction. Furthermore, their response peak currents increased with the potentials scanning speeding up. It is noteworthy that the background currents also enhanced synchronously. To pursue high-signal to noise (S/N), 0.1  $Vs^{-1}$  was recommended as the optimal scanning rate. As shown in Figure 6B, the redox peak currents of DA were proportional to the square root of the scanning rate ( $v^{1/2}$ ), suggesting the electrooxidation of DA is a diffusion-controlled process. There was also a good relationship between the anodic peak currents of UA and the square root of the scanning rate (Figure 6C), indicating a diffusion-limited electrode process for UA oxidation.

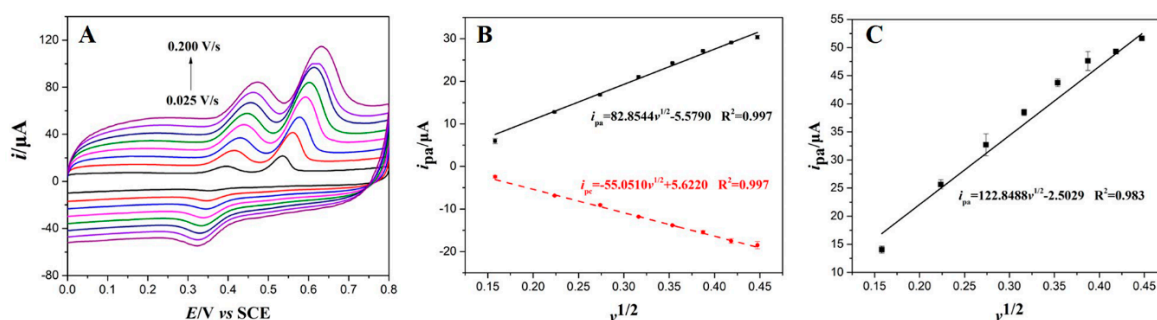


**Figure 6.** (A) CVs of 10  $\mu$ M DA and UA (1:1) at different scanning rates. (B) Linear relationship between the redox peak currents of DA and square root of scanning rates ( $n = 3$ ); (C) Linear relationship between the anodic peak currents of UA and square root of scanning rates ( $n = 3$ ).

### 3.4.3. Influence of Accumulation Parameters

Accumulation can effectively boost the response peak currents of target species, so the influence of accumulation potential and time were also investigated. The anodic peak currents of DA and UA sharply increased with the accumulation potentials shifting from  $-0.4$  V to  $-0.3$  V, then they gradually decreased with a further increase of the accumulation potential (Figure 7A). The highest anodic peak currents of DA and UA were achieved at  $-0.3$  V, so  $-0.3$  V was chosen as the optimal accumulation potential. As presented in Figure 7B, their anodic peak currents gradually enhanced during the first 150 s, then decreased with the prolonging of the accumulation time. Therefore, accumulation was performed at  $-0.3$  V for 150 s in the following experiments.

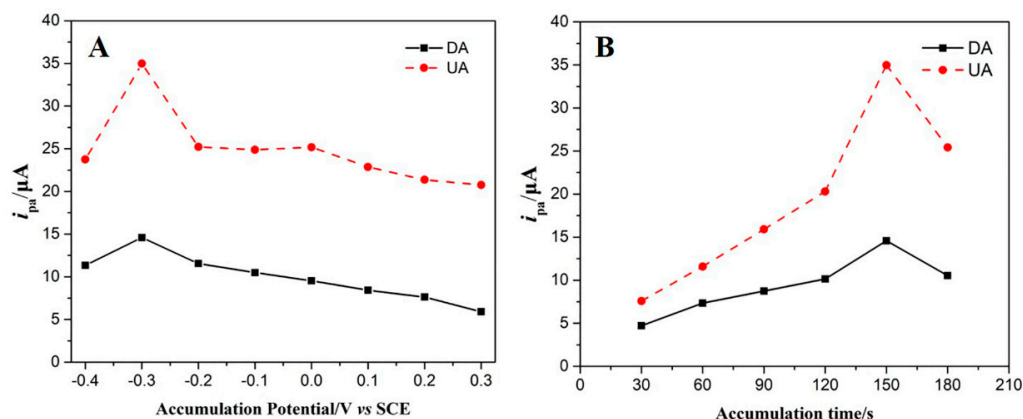


**Figure 7.** Effect of accumulation potential (A) and time (B) on the anodic peak currents of DA and UA.

### 3.5. Individual and Simultaneous Determination of DA and UA

For individual detection of DA and UA at the  $\text{MnO}_2\text{NFs}/\text{NrGO}/\text{GCE}$ , LSVs were measured in the potential range of 0–0.8 V in 0.1 M PBS (pH 3.93). In this case, only the concentrations of the target substance were varied, while the concentrations of the other substance were kept unchanged. As illustrated in Figure 8A,B, there was a good linear relationship between the  $i_{pa}(\text{DA})$  and DA concentrations ranging from 0.4  $\mu\text{M}$  to 10  $\mu\text{M}$ . The linear equation is  $i_{pa}(\text{DA}) = 1.3090C_{\text{DA}} - 0.1953$  ( $R^2 = 0.989$ ). However, the  $i_{pa}(\text{DA})$  were positively proportional to the Napierian logarithm of DA concentrations ( $\ln C_{\text{DA}}$ ) in the concentration range of 10  $\mu\text{M}$ –100  $\mu\text{M}$  (Figure 8C,D). The linear regression equation can be expressed as  $i_{pa}(\text{DA}) = 19.1371\ln C_{\text{DA}} - 32.3044$  ( $R^2 = 0.993$ ). The LOD was estimated as 0.054  $\mu\text{M}$ . Regarding the individual determination of UA, the  $i_{pa}(\text{UA})$  were well-linear to the working concentrations, varying from 0.4  $\mu\text{M}$  to 6.0  $\mu\text{M}$  (Figure 9A,B), with the linear equation of  $i_{pa}(\text{UA}) = 2.4934C_{\text{UA}} - 0.9302$  ( $R^2 = 0.989$ ). At the higher concentration region (6.0  $\mu\text{M}$  to 100  $\mu\text{M}$ ), the  $i_{pa}(\text{UA})$  were positively correlated to the Napierian logarithm of UA concentrations ( $\ln C_{\text{UA}}$ ).

The corresponding linear equation is  $i_{pa}(UA) = 44.3228 \ln C_{UA} - 65.7789$  ( $R^2 = 0.995$ ). The LOD is  $0.062 \mu\text{M}$  for the individual determination of UA. It is noteworthy that the addition of the target biomolecule does not have a notable interference on the electrochemical response signals of the other biomolecule. The results firmly imply that DA and UA can be sensitively and selectively detected at  $\text{MnO}_2\text{NFs/NrGO/GCE}$  in the mixture of DA and UA.

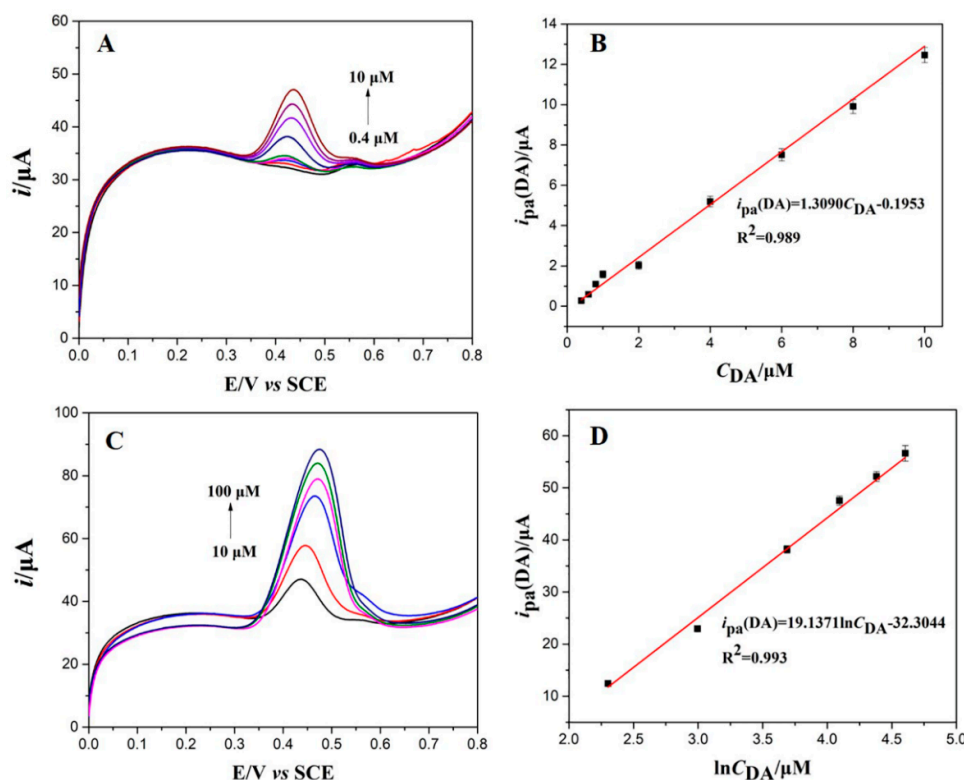


**Figure 8.** Linear scanning voltammetry (LSVs) at the  $\text{MnO}_2\text{NFs/NrGO/GCE}$  in  $0.1 \text{ M PBS}$  ( $\text{pH } 3.93$ ) containing  $1 \mu\text{M UA}$  and various DA concentrations from  $0.4 \mu\text{M}$  to  $10 \mu\text{M}$  (A) and from  $10 \mu\text{M}$  to  $100 \mu\text{M}$  (C); Linear plots of the  $i_{pa}(\text{DA})$  versus the DA concentrations varying from  $0.4 \mu\text{M}$  to  $10 \mu\text{M}$  (B) and from  $10 \mu\text{M}$  to  $100 \mu\text{M}$  (D).

The remarkable electrocatalytic activity of  $\text{MnO}_2\text{NFs/NrGO}$  enables simultaneous detection of DA and UA using the LSV method (Figure 10). Two well-separated anodic peaks belonging to the electrooxidation of DA and UA were observed on LSV curves using  $\text{MnO}_2\text{NFs/NrGO/GCE}$ . Furthermore, LSV responses were resolved into two peaks at  $0.420 \text{ V}$  and  $0.554 \text{ V}$ , respectively. The results demonstrate an excellent discriminability from the two biomolecules in mixture solutions. At the lower concentration region ( $0.02 \mu\text{M}$ – $6.0 \mu\text{M}$ ), the  $i_{pa}(\text{DA})$  and  $i_{pa}(\text{UA})$  enhanced linearly with their concentrations increasing (Figure 10A, B). The linear plots can be expressed as  $i_{pa}(\text{DA}) = 3.0627 C_{\text{DA}} - 0.2848$  ( $R^2 = 0.991$ ), and  $i_{pa}(\text{UA}) = 3.0627 C_{\text{UA}} - 0.2848$  ( $R^2 = 0.990$ ), respectively. However, the  $i_{pa}(\text{DA})$  and  $i_{pa}(\text{UA})$  are positively proportional to the Napierian logarithm of the DA and UA concentrations ( $\ln C_{\text{DA}}$  and  $\ln C_{\text{UA}}$ ) at the higher concentration region from  $6.0 \mu\text{M}$  to  $100 \mu\text{M}$  (Figure 10C, D). The corresponding linear regression equations are  $i_{pa}(\text{DA}) = 16.2222 \ln C_{\text{DA}} - 12.4506$  and  $i_{pa}(\text{UA}) = 37.7032 \ln C_{\text{UA}} - 48.2926$ , respectively. The correlation coefficient is  $0.990$  for both DA and UA. The LODs are calculated to be  $0.036 \mu\text{M}$  and  $0.029 \mu\text{M}$  for DA and UA, respectively. All of the results indicate that the proposed  $\text{MnO}_2\text{NFs/NrGO/GCE}$  featured wider linear detection ranges and a lower LOD for the electrochemical oxidation of DA and UA. The analytical performances were compared to those in previous works (Table 1). Obviously, the sensing parameters of the proposed sensor are comparable to, or even better than, previously reported modified electrodes [7,46–54].

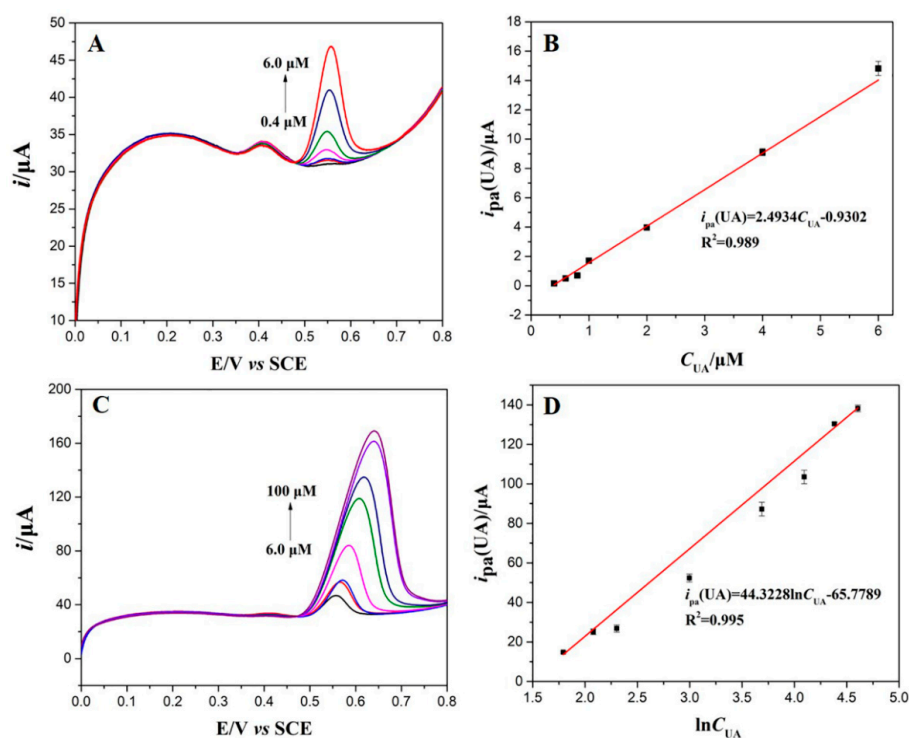


**Figure 9.** (A) LSVs at the MnO<sub>2</sub>NFs/NrGO/GCE in 0.1 M phosphate buffered solution (PBS) (pH 3.93) containing 1 μM DA and various UA concentrations from 0.4 μM to 6.0 μM (A) and from 6.0 μM to 100 μM (C) ( $n = 3$ ); Linear plots of the  $i_{pa}(UA)$  versus the UA concentrations varying from 0.4 μM to 6.0 μM (B) and from 6.0 μM to 100 μM (D) ( $n = 3$ ).

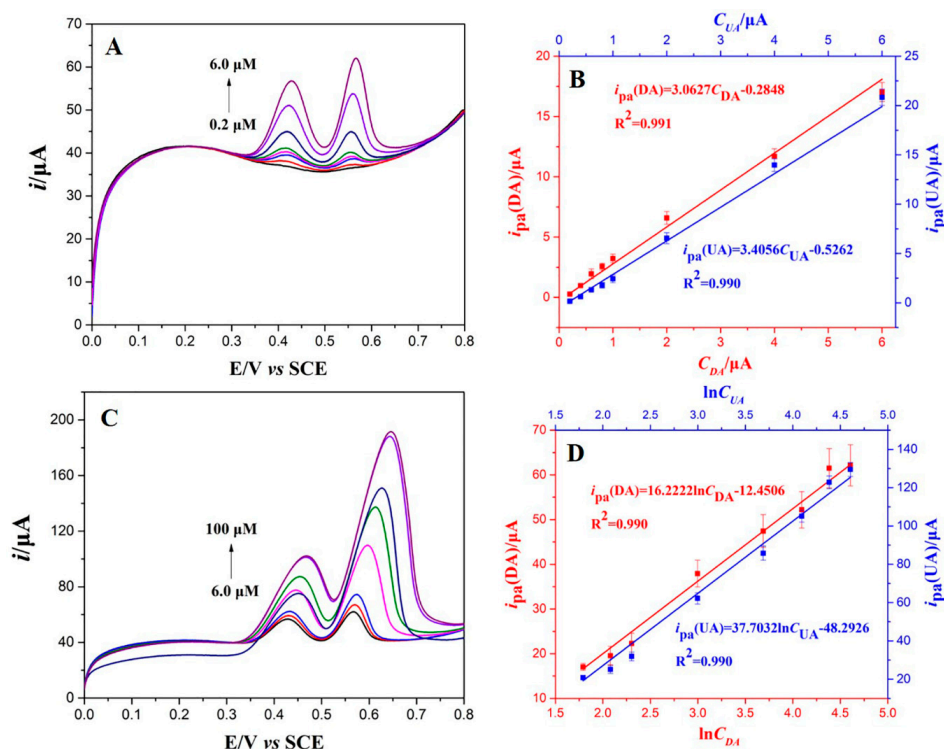


**Figure 10.** (A) LSVs on the MnO<sub>2</sub>NFs/NrGO/GCE in 0.1 MPBS (pH 3.93) containing various concentrations of DA and UA ranging from 0.2 μM to 6.0 μM (A) and from 6.0 μM to 100 μM (C); (B) Plots of the anodic peak currents as the function of DA and UA concentrations in the range of 0.2 μM–6.0 μM ( $n = 3$ ); (D) Plots of the anodic peak currents as the function of DA and UA concentrations in the range of 6.0 μM–100 μM ( $n = 3$ ).

**Table 1.** Comparison sensing performance between previous reports and the proposed MnO<sub>2</sub>NFs/NrGO/GCE for the simultaneous detection of DA and UA.

Electrodes	Methods	Detection Range (μM)		LOD (μM)		Ref.
		DA	UA	DA	UA	
Au/Cu <sub>2</sub> O/rGO/GCE	<sup>a</sup> DPV	10–90	100–900	3.9	6.5	[7]
NrGO/GCE	DPV	0.5–170	0.1–20	0.25	0.045	[46]
Pd/RGO/GCE	DPV	0.45–71	6–469.5	0.18	1.6	[47]
Pt/RGO/GCE	DPV	10–170	10–130	0.25	0.45	[48]
ZnO/SPCE	DPV	0.1–374	0.1–169	0.004	0.00849	[49]
PtNi@MoS <sub>2</sub> /GCE	DPV	0.5–150	0.5–600	0.1	0.1	[50]
Au–Pt/GO–ERGO	DPV	0.0682–49,800	0.125–82,800	0.0207	0.0407	[51]
HFP/GCE	DPV	1–200	20–400	0.016	0.218	[52]
MoS <sub>2</sub> /GCE	DPV	1–900	1–60	0.15	0.06	[53]
ZnO/PANI/rGO/GCE	DPV	0.1–90	0.5–90	0.017	0.12	[54]
MoS <sub>2</sub> /rGO/GCE	DPV	5–545	25–2745	0.05	0.46	[55]
NCNF/GCE	DPV	1–10; 10–200	5–200	0.5	1	[56]
PTPCNs/GCE	DPV	1–100	5–200	0.078	0.17	[57]
MnO <sub>2</sub> NFs/NrGO/GCE	LSV	0.2–6.0; 6.0–100	0.2–6.0; 6.0–100	0.036	0.029	This work

<sup>a</sup> DPV: differential pulse voltammetry.

### 3.6. Selectivity, Repeatability, and Reproducibility Assay

Before real sample detection, the selectivity and repeatability, as well as reproducibility were also evaluated. To assess the anti-interfering ability of the proposed MnO<sub>2</sub>NFs/NrGO/GCE, the LSV responses of the DA and UA in the coexistence of common interfering substances (i.e., ascorbic acid, alanine, citric acid, glutamic acid, cysteine, and lysine) were compared. The relative errors (less than 5%) were accepted even in the presence of 100-fold the above interfering species, demonstrating good selectivity (Figure S1). It is noted that the 100-fold AA have no obvious interfering because of the well-separated peak potential between AA and DA ( $\Delta E_p = 0.260$  V). To check the repeatability, eight successive determinations of 1 μM DA and UA (1:1) were also performed. The relative standard deviation (RSD) for DA and UA were 6.35% and 5.32%, respectively, indicating good repeatability. To examine electrode reproducibility, the anodic peak currents of 1 μM DA and UA were recorded at five MnO<sub>2</sub>NFs/NrGO/GCEs, which were prepared by similar procedure. The RSD of the anodic peaks were 6.02% and 4.70% for DA and UA respectively, showing that the electrode preparation have excellent reproducibility.

### 3.7. Determination of DA and UA in Human Serum Samples

To validate practicability, the concentrations of DA and UA in human serum samples were also detected on MnO<sub>2</sub>NFs/NrGO/GCE. The determination results were calculated from the calibration curves (Table 2). To further validate the precision of the proposed sensor, a series of known concentration solutions of DA and UA were spiked with the serum samples to figure out the recovery. The recoveries are 96.2–105.6% and 96.2–104.9% for DA and UA respectively, verifying that biological matrixes, like human serum, do not influence the simultaneous detection of DA and UA.

**Table 2.** Detection results of DA and UA in human serum samples using MnO<sub>2</sub>NFs/NrGO/GCE ( $n = 3$ ).

<sup>a</sup> Samples	Detected (μM)	Added (μM)	Found (μM)	RSD (%)	Recovery (%)	
Serum	DA	<sup>b</sup> ND	20	18.98	4.25	94.9
			40	38.48	3.76	96.2
	UA	21.8	20	42.92	2.98	105.6
			40	63.74	2.45	104.9

<sup>a</sup> The human serum samples were detected at 10-fold dilution. <sup>b</sup> Not detected.

#### 4. Conclusions

In summary, this paper reported the facile synthesis of MnO<sub>2</sub>NFs/NrGO nanocomposites and their application on the simultaneous determination of DA and UA. The electrochemical measurements indicated that the MnO<sub>2</sub>NFs/NrGO composites possess a large, effective electroactive area and low-charge transfer resistance. MnO<sub>2</sub>NFs/NrGO/GCE showed superb catalytic capacity toward the electrooxidation of DA and UA, attributing to the synergistic effect from MnO<sub>2</sub>NFs and NrGO sheets. The anodic peak currents of DA and UA increased linearly with their concentrations varying from 0.2 μM to 6.0 μM. However, their anodic peak currents were highly correlated to the Napierian logarithm of their concentrations, ranging from 6.0 μM to 100 μM. The LODs were 0.036 μM and 0.029 μM for DA and UA, respectively. Furthermore, the proposed sensor successfully realized DA and UA detection in human serum samples with satisfactory recovery. Combining with prominent advantages such as facile preparation, high sensitivity, good selectivity, repeatability, and reproducibility, the proposed MnO<sub>2</sub>NFs/NrGO nanocomposites have become the most competitive candidates for the simultaneous determination of DA and UA in various real samples.

**Supplementary Materials:** The following are available online at <http://www.mdpi.com/2079-4991/9/6/847/s1>, Figure S1: The anodic peak currents of 1 μM DA and UA in the presence of 100-fold alanine (AL), glutamic acid (GA), ascorbic acid (AA), lysine (LY) and citric acid (CA).

**Author Contributions:** X.W., S.Y. conceived and designed the experiments; X.W., S.Y., and Z.C. performed the experiments; X.W., S.Y., Z.C., Y.Y., and Y.X. analyzed the data; Q.H., G.L., and J.L. contributed reagents/materials/analysis tools; X.W. and S.Y. wrote the original draft; G.L. revised the manuscript.

**Funding:** This work was supported by the Undergraduates' Innovation Experiment Program of Hunan Province (No. 2018649), Natural Science Foundation of Hunan Province (No. 2019JJ50127, 2018JJ3134), National Natural Science Foundation of China (No. 61703152), Scientific Research Foundation of Hunan Provincial Education Department (18A273, 18C0522), Project of Science and Technology Plan of Zhuzhou (201707201806).

**Acknowledgments:** We sincerely express our thanks to Zhuzhou People's Hospital for offering human serum samples.

**Conflicts of Interest:** The authors declare no conflicts of interest.

#### References

1. He, Q.; Liu, J.; Liang, J.; Liu, X.; Li, W.; Liu, Z.; Ding, Z.; Tuo, D. Towards improvements for penetrating the blood–brain barrier—Recent progress from a material and pharmaceutical perspective. *Cells* **2018**, *7*, 24. [[CrossRef](#)] [[PubMed](#)]
2. Dalley, J.W.; Roiser, J.P. Dopamine, serotonin and impulsivity. *Neuroscience* **2012**, *215*, 42–58. [[CrossRef](#)] [[PubMed](#)]
3. Carlsson, A. Does dopamine play a role in schizophrenia? *Psychol. Med.* **1977**, *7*, 583–597. [[CrossRef](#)] [[PubMed](#)]
4. Zhang, M.; Liao, C.; Yao, Y.; Liu, Z.; Gong, F.; Yan, F. High-performance dopamine sensors based on whole-graphene solution-gated transistors. *Adv. Funct. Mater.* **2014**, *24*, 978–985. [[CrossRef](#)]
5. Wightman, R.M.; May, L.J.; Michael, A.C. Detection of dopamine dynamics in the brain. *Anal. Chem.* **1988**, *60*, 769A–779A. [[CrossRef](#)]
6. Jindal, K.; Tomar, M.; Gupta, V. Nitrogen-doped zinc oxide thin films biosensor for determination of uric acid. *Analyst* **2013**, *138*, 4353–4362. [[CrossRef](#)]
7. Aparna, T.K.; Sivasubramanian, R.; Dar, M.A. One-pot synthesis of Au-Cu<sub>2</sub>O/rGO nanocomposite based electrochemical sensor for selective and simultaneous detection of dopamine and uric acid. *J. Alloys Compd.* **2018**, *741*, 1130–1141. [[CrossRef](#)]
8. Sharaf El Din, U.A.A.; Salem, M.M.; Abdulazim, D.O. Uric acid in the pathogenesis of metabolic, renal, and cardiovascular diseases: A review. *J. Adv. Res.* **2017**, *8*, 537–548. [[CrossRef](#)]
9. Huang, C.; Chen, X.; Lu, Y.; Yang, H.; Yang, W. Electrogenerated chemiluminescence behavior of peptide nanovesicle and its application in sensing dopamine. *Biosens. Bioelectron.* **2015**, *63*, 478–482. [[CrossRef](#)]
10. Xiang, L.-W.; Li, J.; Lin, J.M.; Li, H.F. Determination of gouty arthritis' biomarkers in human urine using reversed-phase high-performance liquid chromatography. *J. Pharm. Anal.* **2014**, *4*, 153–158. [[CrossRef](#)]

11. Lin, L.; Qiu, P.; Yang, L.; Cao, X.; Jin, L. Determination of dopamine in rat striatum by microdialysis and high-performance liquid chromatography with electrochemical detection on a functionalized multi-wall carbon nanotube electrode. *Anal. Bioanal. Chem.* **2006**, *384*, 1308–1313. [[CrossRef](#)] [[PubMed](#)]
12. Zhao, D.; Song, H.; Hao, L.; Liu, X.; Zhang, L.; Lv, Y. Luminescent ZnO quantum dots for sensitive and selective detection of dopamine. *Talanta* **2013**, *107*, 133–139. [[CrossRef](#)] [[PubMed](#)]
13. Moghadam, M.R.; Dadfarnia, S.; Shabani, A.M.H.; Shahbazikhah, P. Chemometric-assisted kinetic–spectrophotometric method for simultaneous determination of ascorbic acid, uric acid, and dopamine. *Anal. Biochem.* **2011**, *410*, 289–295. [[CrossRef](#)] [[PubMed](#)]
14. Kumbhat, S.; Shankaran, D.R.; Kim, S.J.; Gobi, K.V.; Joshi, V.; Miura, N. Surface plasmon resonance biosensor for dopamine using D3 dopamine receptor as a biorecognition molecule. *Biosens. Bioelectron.* **2007**, *23*, 421–427. [[CrossRef](#)] [[PubMed](#)]
15. Liu, S.; Yan, J.; He, G.; Zhong, D.; Chen, J.; Shi, L.; Zhou, X.; Jiang, H. Layer-by-layer assembled multilayer films of reduced graphene oxide/gold nanoparticles for the electrochemical detection of dopamine. *J. Electroanal. Chem.* **2012**, *672*, 40–44. [[CrossRef](#)]
16. He, Q.; Liu, J.; Liu, X.; Li, G.; Chen, D.; Deng, P.; Liang, J. A promising sensing platform toward dopamine using MnO<sub>2</sub> nanowires/electro-reduced graphene oxide composites. *Electrochim. Acta* **2019**, *296*, 683–692. [[CrossRef](#)]
17. He, Q.; Liu, J.; Liu, X.; Li, G.; Deng, P.; Liang, J. Manganese dioxide nanorods/electrochemically reduced graphene oxide nanocomposites modified electrodes for cost-effective and ultrasensitive detection of Amaranth. *Colloids Surf. B* **2018**, *172*, 565–572. [[CrossRef](#)] [[PubMed](#)]
18. He, Q.; Liu, J.; Liu, X.; Li, G.; Deng, P.; Liang, J.; Chen, D. Sensitive and selective detection of tartrazine based on TiO<sub>2</sub>-electrochemically reduced graphene oxide composite-modified electrodes. *Sensors* **2018**, *18*, 1911. [[CrossRef](#)] [[PubMed](#)]
19. He, Q.; Liu, J.; Liu, X.; Li, G.; Chen, D.; Deng, P.; Liang, J. Fabrication of amine-modified magnetite-electrochemically reduced graphene oxide nanocomposite modified glassy carbon electrode for sensitive dopamine determination. *Nanomaterials* **2018**, *8*, 194. [[CrossRef](#)]
20. He, Q.; Liu, J.; Liu, X.; Li, G.; Deng, P.; Liang, J. Preparation of Cu<sub>2</sub>O-reduced graphene nanocomposite modified electrodes towards ultrasensitive dopamine detection. *Sensors* **2018**, *18*, 199. [[CrossRef](#)]
21. Chen, L.X.; Zheng, J.N.; Wang, A.J.; Wu, L.-J.; Chen, J.R.; Feng, J.J. Facile synthesis of porous bimetallic alloyed PdAg nanoflowers supported on reduced graphene oxide for simultaneous detection of ascorbic acid, dopamine, and uric acid. *Analyst* **2015**, *140*, 3183–3192. [[CrossRef](#)] [[PubMed](#)]
22. Dong, S.; Xi, J.; Wu, Y.; Liu, H.; Fu, C.; Liu, H.; Xiao, F. High loading MnO<sub>2</sub> nanowires on graphene paper: Facile electrochemical synthesis and use as flexible electrode for tracking hydrogen peroxide secretion in live cells. *Anal. Chim. Acta* **2015**, *853*, 200–206. [[CrossRef](#)]
23. Yang, P.; Hou, Z.; Hang, Y.; Liu, Y.N. Hierarchical architecture of nanographene-coated rice-like manganese dioxide nanorods/graphene for enhanced electrocatalytic activity toward hydrogen peroxide reduction. *Mater. Sci. Semicond. Process.* **2015**, *40*, 176–182.
24. Zeng, F.; Yang, P.; Yong, Y.; Li, Q.; Li, G.; Hou, Z.; Gang, G. Facile construction of Mn<sub>3</sub>O<sub>4</sub>-MnO<sub>2</sub> hetero-nanorods/graphene nanocomposite for highly sensitive electrochemical detection of hydrogen peroxide. *Electrochim. Acta* **2016**, *196*, 587–596. [[CrossRef](#)]
25. Zhang, S.; Zheng, J. Synthesis of single-crystal  $\alpha$ -MnO<sub>2</sub> nanotubes-loaded Ag@C core-shell matrix and their application for electrochemical sensing of nonenzymatic hydrogen peroxide. *Talanta* **2016**, *159*, 231–237. [[CrossRef](#)] [[PubMed](#)]
26. Mahmoudian, M.R.; Alias, Y.; Basirun, W.J.; Pei, M.W.; Sookhakian, M. Facile preparation of MnO<sub>2</sub> nanotubes/reduced graphene oxide nanocomposite for electrochemical sensing of hydrogen peroxide. *Sens. Actuators B* **2014**, *201*, 526–534. [[CrossRef](#)]
27. Huang, J.; Qiang, Z.; Wang, L. Ultrasensitive electrochemical determination of Ponceau 4R with a novel  $\epsilon$ -MnO<sub>2</sub> microspheres/chitosan modified glassy carbon electrode. *Electrochim. Acta* **2016**, *206*, 176–183. [[CrossRef](#)]
28. Wang, H.E.; Qian, D. Synthesis and electrochemical properties of  $\alpha$ -MnO<sub>2</sub> microspheres. *Mater. Chem. Phys.* **2008**, *109*, 399–403. [[CrossRef](#)]

29. Xue, S.; Jing, P.; Xu, W. Hemin on graphene nanosheets functionalized with flower-like MnO<sub>2</sub> and hollow AuPd for the electrochemical sensing lead ion based on the specific DNAzyme. *Biosens. Bioelectron.* **2016**, *86*, 958–965. [[CrossRef](#)] [[PubMed](#)]
30. Ming, Y.W.; Wei, Z.; Lin, M.; Ma, J.J.; Dong, E.Z.; Zhi, W.T.; Chen, J. Enhanced simultaneous detection of ractopamine and salbutamol—Via electrochemical-facial deposition of MnO<sub>2</sub> nanoflowers onto 3D RGO/Ni foam templates. *Biosens. Bioelectron.* **2016**, *78*, 259–266.
31. Gan, T.; Shi, Z.; Deng, Y.; Sun, J.; Wang, H. Morphology-dependent electrochemical sensing properties of manganese dioxide-graphene oxide hybrid for guaiacol and vanillin. *Electrochim. Acta* **2014**, *147*, 157–166. [[CrossRef](#)]
32. Ray, C.; Dutta, S.; Roy, A.; Sahoo, R.; Pal, T. Redox mediated synthesis of hierarchical Bi<sub>2</sub>O<sub>3</sub>/MnO<sub>2</sub> nanoflowers: A Non-Enzymatic Hydrogen Peroxide Electrochemical Sensor. *Dalton Trans.* **2016**, *45*, 4780–4790. [[CrossRef](#)] [[PubMed](#)]
33. Yang, B.; Wang, J.; Duan, B.; Zhu, M.; Yang, P.; Du, Y. A three dimensional Pt nanodendrite/graphene/MnO<sub>2</sub> nanoflower modified electrode for the sensitive and selective detection of dopamine. *J. Mater. Chem. B* **2015**, *3*, 7440–7448. [[CrossRef](#)]
34. Fan, H.; Yan, L.; Dan, W.; Ma, H.; Mao, K.; Fan, D.; Du, B. Electrochemical bisphenol A sensor based on N-doped graphene sheets. *Anal. Chim. Acta* **2012**, *711*, 24–28. [[CrossRef](#)] [[PubMed](#)]
35. Wang, H.; Maiyalagan, T.; Wang, X. Review on recent progress in nitrogen-doped graphene: Synthesis, Characterization, and its potential applications. *ACS Catal.* **2012**, *2*, 781–794. [[CrossRef](#)]
36. Paraknowitsch, J.P.; Thomas, A. Doping carbons beyond nitrogen: An Overview of Advanced Heteroatom Doped Carbons with Boron, sulphur and phosphorus for energy applications. *Energy Environ. Sci.* **2013**, *6*, 2839–2855. [[CrossRef](#)]
37. Yang, Z.; Zheng, X.; Zheng, J. A facile one-step synthesis of Fe<sub>2</sub>O<sub>3</sub>/nitrogen-doped reduced graphene oxide nanocomposite for enhanced electrochemical determination of dopamine. *J. Alloys Compd.* **2017**, *709*, 581–587. [[CrossRef](#)]
38. Chen, R.; Wang, Y.; Yang, L.; Li, J. Selective electrochemical detection of dopamine using nitrogen-doped graphene/manganese monoxide composites. *RSC Adv.* **2015**, *5*, 85065–85072. [[CrossRef](#)]
39. Bard, A.J.; Faulkner, L.R.; Bard, A.; Faulkner, L. *Electrochemical Methods: Fundamentals and Applications*; Wiley: New York, NY, USA, 2001; pp. 669–676.
40. Li, G.; Wang, S.; Duan, Y.Y. Towards conductive-gel-free electrodes: Understanding the wet electrode, semi-dry electrode and dry electrode-skin interface impedance using electrochemical impedance spectroscopy fitting. *Sens. Actuators B* **2018**, *277*, 250–260. [[CrossRef](#)]
41. Li, G.; Wang, S.; Duan, Y.Y. Towards gel-free electrodes: A systematic study of electrode-skin impedance. *Sens. Actuators B* **2017**, *241*, 1244–1255. [[CrossRef](#)]
42. Li, G.; Zhang, D.; Wang, S.; Duan, Y.Y. Novel passive ceramic based semi-dry electrodes for recording electroencephalography signals from the hairy scalp. *Sens. Actuators B* **2016**, *237*, 167–178. [[CrossRef](#)]
43. Wang, Y.; Li, Y.; Tang, L.; Lu, J.; Li, J. Application of graphene-modified electrode for selective detection of dopamine. *Electrochem. Commun.* **2009**, *11*, 889–892. [[CrossRef](#)]
44. Naderi, H.R.; Norouzi, P.; Ganjali, M.R. Electrochemical Study of a Novel High Performance Supercapacitor Based on MnO<sub>2</sub>/Nitrogen-Doped Graphene Nanocomposite. *Appl. Surf. Sci.* **2016**, *366*, 552–560. [[CrossRef](#)]
45. Zare, H.R.; Rajabzadeh, N.; Nasirizadeh, N.; Ardakani, M.M. Voltammetric studies of an oracet blue modified glassy carbon electrode and its application for the simultaneous determination of dopamine, ascorbic acid and uric acid. *J. Electroanal. Chem.* **2006**, *589*, 60–69. [[CrossRef](#)]
46. Sheng, Z.-H.; Zheng, X.-Q.; Xu, J.-Y.; Bao, W.-J.; Wang, F.-B.; Xia, X.-H. Electrochemical sensor based on nitrogen doped graphene: Simultaneous Determination of Ascorbic acid, dopamine and uric acid. *Biosens. Bioelectron.* **2012**, *34*, 125–131. [[CrossRef](#)] [[PubMed](#)]
47. Wang, J.; Yang, B.; Zhong, J.; Yan, B.; Zhang, K.; Zhai, C.; Shiraishi, Y.; Du, Y.; Yang, P. Dopamine and uric acid electrochemical sensor based on a glassy carbon electrode modified with cubic Pd and reduced graphene oxide nanocomposite. *J. Colloid Interface Sci.* **2017**, *497*, 172–180. [[CrossRef](#)]
48. Xu, T.-Q.; Zhang, Q.L.; Zheng, J.-N.; Lv, Z.Y.; Wei, J.; Wang, A.J.; Feng, J.J. Simultaneous determination of dopamine and uric acid in the presence of ascorbic acid using Pt nanoparticles supported on reduced graphene oxide. *Electrochim. Acta* **2014**, *115*, 109–115. [[CrossRef](#)]

49. Kogularasu, S.; Akilarasan, M.; Chen, S.-M.; Chen, T.W.; Lou, B.S. Urea-based morphological engineering of ZnO; for the biosensing enhancement towards dopamine and uric acid in food and biological samples. *Mater. Chem. Phys.* **2019**, *227*, 5–11. [[CrossRef](#)]
50. Ma, L.; Zhang, Q.; Wu, C.; Zhang, Y.; Zeng, L. PtNi bimetallic nanoparticles loaded MoS<sub>2</sub> nanosheets: Preparation and electrochemical sensing application for the detection of dopamine and uric acid. *Anal. Chim. Acta* **2019**, *1055*, 17–25. [[CrossRef](#)]
51. Liu, Y.; She, P.; Gong, J.; Wu, W.; Xu, S.; Li, J.; Zhao, K.; Deng, A. A novel sensor based on electrodeposited Au–Pt bimetallic nano-clusters decorated on graphene oxide (GO)–electrochemically reduced GO for sensitive detection of dopamine and uric acid. *Sens. Actuators B* **2015**, *221*, 1542–1553. [[CrossRef](#)]
52. Emran, M.Y.; Shenashen, M.A.; Abdelwahab, A.A.; Abdelmottaleb, M.; Khairy, M.; El-Safty, S.A. Nano-hexagonal Fe<sub>2</sub>O<sub>3</sub> electrode for one-step selective monitoring of dopamine and uric acid in biological samples. *Electrocatalysis* **2018**, *9*, 514–525. [[CrossRef](#)]
53. Yin, A.; Wei, X.; Cao, Y.; Li, H. High-quality molybdenum disulfide nanosheets with 3D structure for electrochemical sensing. *Appl. Surf. Sci.* **2016**, *385*, 63–71. [[CrossRef](#)]
54. Ghanbari, K.; Moloudi, M. Flower-like ZnO decorated polyaniline/reduced graphene oxide nanocomposites for simultaneous determination of dopamine and uric acid. *Anal. Biochem.* **2016**, *512*, 91–102. [[CrossRef](#)] [[PubMed](#)]
55. Xing, L.; Ma, Z. A glassy carbon electrode modified with a nanocomposite consisting of MoS<sub>2</sub> and reduced graphene oxide for electrochemical simultaneous determination of ascorbic acid, dopamine, and uric acid. *Microchim. Acta* **2016**, *183*, 257–263. [[CrossRef](#)]
56. Sun, J.; Li, L.; Zhang, X.; Liu, D.; Lv, S.; Zhu, D.; Wu, T.; You, T. Simultaneous determination of ascorbic acid, dopamine and uric acid at a nitrogen-doped carbon nanofiber modified electrode. *RSC Adv.* **2015**, *5*, 11925–11932. [[CrossRef](#)]
57. Ahammad, A.J.S.; Odhikari, N.; Shah, S.S.; Hasan, M.M.; Islam, T.; Pal, P.R.; Ahmed Qasem, M.A.; Aziz, M.A. Porous tal palm carbon nanosheets: Preparation, characterization and application for the simultaneous determination of dopamine and uric acid. *Nanoscale Adv.* **2019**, *1*, 613–626. [[CrossRef](#)]



© 2019 by the authors. Licensee MDPI, Basel, Switzerland. This article is an open access article distributed under the terms and conditions of the Creative Commons Attribution (CC BY) license (<http://creativecommons.org/licenses/by/4.0/>).